Nanoscale

PAPER

View Article Online
View Journal | View Issue



Cite this: *Nanoscale*, 2023, **15**, 14669

# Built-in tensile strain dependence on the lateral size of monolayer $MoS_2$ synthesized by liquid precursor chemical vapor deposition†

L. Seravalli, [a] F. Esposito,[a,b] M. Bosi, [a] L. Aversa, [c] G. Trevisi,[a] R. Verucchi, [c] L. Lazzarini,[a] F. Rossi [a] and F. Fabbri *[d]

Received 12th April 2023,
Accepted 14th August 2023

DOI: 10.1039/d3nr01687k

rsc.li/nanoscale

Strain engineering is an efficient tool to tune and tailor the electrical and optical properties of 2D materials. The built-in strain can be tuned during the synthesis process of a two-dimensional semiconductor, such as molybdenum disulfide, by employing different growth substrates with peculiar thermal properties. In this work, we demonstrate that the built-in strain of $MoS_2$ monolayers, grown on a $SiO_2$/Si substrate by liquid precursor chemical vapor deposition, is mainly dependent on the size of the monolayer. In fact, we identify a critical size equal to 20 μm, from which the built-in strain increases drastically. The built-in strain is the maximum for a 60 μm sized monolayer, leading to 1.2% tensile strain with a partial release of strain close to the monolayer triangular vertexes due to the formation of nanocracks. These findings also imply that the standard method for evaluation of the number of layers based on the Raman mode separation can become unreliable for highly strained monolayers with a lateral size above 20 μm.



## Introduction

Strain engineering is an efficient tool to tune and tailor the electrical and optical properties of 2D materials since their electronic band structures are highly sensitive to mechanical deformation.[1–8] Among the different classes of 2D materials, semiconducting transition metal dichalcogenides (TMDs) have demonstrated the most interesting and surprising modifications of electronic properties induced by the application of strain.[9,10] For instance, strain can induce the indirect-to-direct bandgap transition in multilayer $WSe_2$ flakes,[11] while the opposite transition (the direct-to-indirect transition) can occur in monolayer TMDs.[12,13] With regard to optical properties, local strain application can induce exciton funneling,[14,15] efficient exciton to trion conversion[16] or the formation of a new hybrid state of dark and localized excitons.[17]

It is worth noting that TMD monolayers can withstand high tensile strains before breaking, as high as 10% for molybdenum based[18,19] and 19% for tungsten based[20] exfoliated monolayers.

Different approaches have been employed for the application of external stress to 2D materials: the most employed one is based on the use of bendable and stretchable polymeric substrates.[21–28] where it is possible to apply mainly uniaxial strain to 2D materials. This approach is mostly used in the fabrication of origami-like[29] and kirigami-like[30,31] $MoS_2$ based devices, such as strain sensors or optoelectronic devices. A similar approach has been employed to fabricate human eye mimicking photodetectors.[32] Another widely used method is the transfer of a 2D material on a patterned non-planar substrate for inducing localized strain, resulting in a local change of the band structure. The substrate can present insulating[33–36] or semiconducting[37,38] structures, namely stressors, that can apply a large local strain degree at their top. This large localized strain application modifies the band structure of 2D semiconducting materials, enabling efficient charge collection, desirable for bright single photon emission.[35,36] A high degree of strain is also achieved by suspending 2D membranes on hole patterned substrates.[39] A local strain increase can be achieved on suspended membranes using different approaches: using an AFM tip,[40] applying an external gas pressure[41] or applying a gate voltage between a suspended monolayer membrane and an electrode below.[17] An additional novel approach to apply strain to TMD heterostructures is the employment of polymeric artificial muscles, that taking advantage of the low friction between different 2D materials can apply a tensile strain in van der Waals heterostructures.[42]

[a]*Institute of Materials for Electronics and Magnetism (IMEM-CNR), Parco Area delle Scienze 37/a, 43124 Parma, Italy*
[b]*Department of Mathematical, Physical and Computer Sciences, University of Parma, Parco Area delle Scienze 7/a, 43124 Parma, Italy*
[c]*Institute of Materials for Electronics and Magnetism (IMEM-CNR), FBK Trento unit, Via alla Cascata 56/C, 38123 Povo, Trento, Italy*
[d]*NEST, Istituto Nanoscienze – CNR, Scuola Normale Superiore, Piazza San Silvestro 12, 56127 Pisa, Italy. E-mail: filippo.fabbri@nano.cnr.it*
† Electronic supplementary information (ESI) available. See DOI: https://doi.org/10.1039/d3nr01687k

The strain tuning during the chemical vapor deposition (CVD) process of 2D materials has also been demonstrated.[43–45] This method relies on the mismatch of the thermal expansion coefficient (TEC) between the substrate and the 2D material.[4] For instance, monolayer $WSe_2$ with built-in strains ranging from 1% tensile to compressive 0.2% was obtained using different growth substrates. The TEC approach has also been employed in order to synthesize strained $WS_2$ on quartz with an oriented array of wrinkles.[46] In addition, strain induced buckling has been recently identified as a possible cause of threefold symmetric domain formation in hexagonal shaped $WS_2$ monolayers.[47] In the case of $MoS_2$, the modification of strain and doping using different growth substrates has been demonstrated, where the maximum built-in tensile strain is found to be 0.4% with a $SiO_2$ growth substrate.[48]

In this work, we demonstrate the dependence of the tensile strain as a function of the lateral size of sharp-vertex shaped $MoS_2$ monolayers grown on a standard 300 nm thick $SiO_2$/Si substrate by liquid precursor chemical vapor deposition. The built-in strain is demonstrated and evaluated by scanning Raman and photoluminescence spectroscopy. Monolayer $MoS_2$, with a lateral size below 20 μm, presents a built-in compressive strain of 0.3%, while the flakes with the largest lateral size (60 μm) are more strained, reaching an upper limit of 1.2%. It is worth noting that such flakes are affected by nanocracks close to the vertexes, revealing a partial release of the strain down to 0.7%. The built-in strain affects the optical properties; in particular, the highly strained flakes show quenching and red-shifting of the excitonic emissions of $MoS_2$.

## Results and discussion

Fig. 1 illustrates the outcome of the CVD synthesis at increasing temperature using a solution containing a molybdenum liquid precursor. In particular, the sketch (Fig. 1a) shows the deposition of the precursor solution on the $SiO_2$/Si growth substrate by spin coating, carried out for 30 s at 3000 rpm, of the precursor solution. This solution has three main components: a 3 mM solution of ammonium molybdate tetrahydrate (AMT), a 62.5 mM solution of sodium hydroxide (NaOH) and a 0.4 mM solution of iodixanol (Optiprep). Atomic force microscopy (AFM) was employed to study the number of layers composing the flakes and their lateral size. It is worth noting that the flakes obtained with the liquid precursor CVD have the sharp-vertex triangular shape.[49] The lateral size data are reported in Fig. 1b, which highlights the increase of the flake size with the growth temperature. The flakes, grown at 810 °C, present an average lateral size of (15.1 ± 3.0) μm, while the flakes synthesized at 820 °C present an average lateral size of (24.1 ± 4.9) μm. The maximum lateral size, (58.2 ± 5.7) μm, is obtained when the growth process is carried out at 830 °C. Fig. 1c–e present the representative AFM topographical map of the flake obtained at increasing temperature. All the flakes,

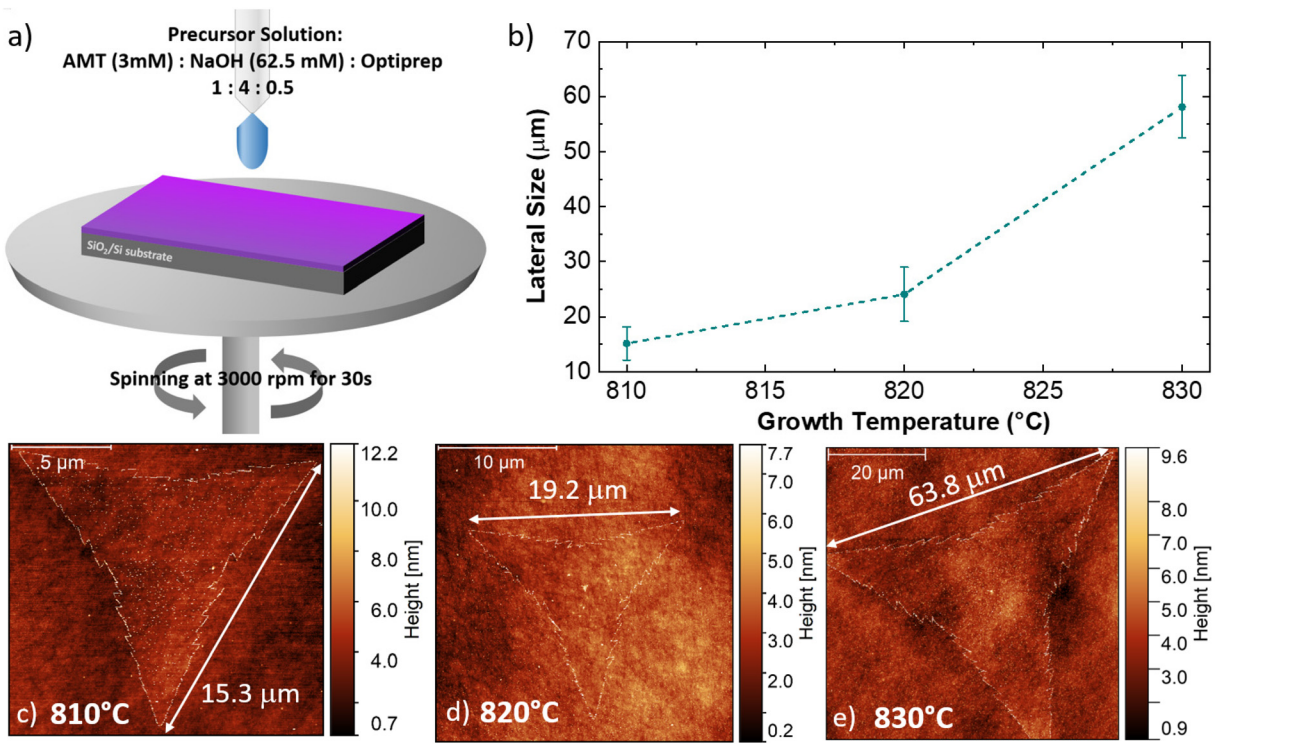


Fig. 1 (a) Illustrative sketch of the substrate preparation prior to the growth process. (b) Dependence of the $MoS_2$ monolayer lateral size *versus* the growth temperature of the CVD process. (c), (d) and (e) Representative AFM topographic maps of the $MoS_2$ flake grown at different temperatures. The lateral size of the flake (white arrow) is 15.3 μm, 19.2 μm and 63.8 μm in the case of 810 °C, 820 °C and 830 °C growth temperatures, respectively.

grown at the different temperatures, present fractal saw-toothed edges, which are probably mediated by a diffusion-limited-aggregation (DLA) regime.[50,51] In addition, the flake edges present nanoparticle decoration. Such an effect is directly connected with the employment of the liquid precursor, since the nanoparticles are composed of precursor byproducts, such as sodium oxide ($Na_2O$).[52]

The AFM topographic maps, acquired on the edge of the flakes, are reported in Fig. 2. The main purpose of such analysis is the evaluation of the number of layers of the $MoS_2$ flake and the morphological analysis of the nanoparticles (NPs) decorating the flake edges. The topographical analysis reveals the presence of nanoparticles of smaller size inside the $MoS_2$ flake and on the $SiO_2$ substrate. All the $MoS_2$ flakes are monolayer: the height profiles reported on the different panels, reveal a flake thickness of 0.7–0.8 nm, the standard thickness of $MoS_2$ monolayer.[53–56] Cross-sectional TEM analysis is reported in Fig. S1,† confirming the monolayer nature of $MoS_2$ obtained at 830 °C. It is worth noting that all the height profiles are acquired in the area of the flake not affected by the nanoparticles and the flakes synthesized at 810 °C and 820 °C present a few nanometer thick step on the edge, similarly to $WS_2$ flakes grown by the CVD process using a tungsten liquid precursor.[47] This effect is due to a strain induced delamination of the ML edges. The nanoparticles decorating the flake edges present a similar diameter, (26 ± 7) nm, while the height increases on increasing the growth temperature. In fact, the height of the nanoparticles varies from (8 ± 2) nm at 810 °C to (18 ± 5) nm at 830 °C, indicating that temperature has an important role in the formation of precursor byproducts. The density of the nanoparticles increases in the case of the growth carried out at 830 °C with an average linear density of nanoparticles of 32 NPs per μm, while the linear density decreases to 22 NPs per μm for the synthesis at lower temperatures. The statistical analysis of the NP morphology is reported in Fig. S2.†

Fig. 3 presents the Raman characterization of the monolayer $MoS_2$, synthesized at increasing temperatures. The representative Raman spectrum (Fig. 3a), acquired at the center of the flake grown at 810 °C (black line), presents the standard $MoS_2$ Raman modes, $E_{2g}$, at 383.6 $cm^{-1}$ and $A_{1g}$, at 403.5 $cm^{-1}$, with a Raman mode separation of 19.9 $cm^{-1}$. The $A_{1g}$ mode corresponds to the sulfur atoms oscillating in antiphase out-of-plane and the $E_{2g}$ mode is related to the sulfur and molybdenum atoms oscillating in antiphase parallel to the crystal plane.

The separation of the Raman modes below 20 $cm^{-1}$ is the standard benchmark of monolayer $MoS_2$.[23,57,58] However, this analysis of the $MoS_2$ monolayer grown at higher temperature demonstrates that both the $MoS_2$ Raman modes are shifted. In fact, in case of the flake grown at 820 °C (red line) the $E_{2g}$ and the $A_{1g}$ modes appear at 382.5 $cm^{-1}$ and at 404 $cm^{-1}$, respectively. The separation of the Raman mode is 21.5 $cm^{-1}$, a value standardly reported for bilayer $MoS_2$.[57,58] For the flakes grown at the 830 °C (green line) the $A_{1g}$ mode is still set at 404 $cm^{-1}$, while the $E_{2g}$ presents an additional shift down to 380.2 $cm^{-1}$. The separation of the Raman modes is 23.8 $cm^{-1}$, the standard benchmark of few-layers $MoS_2$.[57,58] The larger shift of the $E_{2g}$ mode is a symptom of the presence of strain because the $A_{1g}$ mode is less affected than the $E_{2g}$ mode, being the $A_{1g}$ mode related to the out-of-plane vibration with respect to the $E_{2g}$ mode. In particular, the different response to strain of the two $MoS_2$ Raman modes is reflected in the different Grüneisen parameter of each vibrational mode: $\gamma_{E_{2g}} = 0.68$ and $\gamma_{A_{1g}} = 0.21$.[26,41,59] Another clue of the presence of built-in strain applied to the $MoS_2$ grown at high temperature is the broadening of the $E_{2g}$ mode, whose full width at half maximum (FWHM) is from 2.5 $cm^{-1}$ (810 °C grown monolayers) up to 10.4 $cm^{-1}$ (830 °C grown monolayer);[26] in fact, the application of strain induces the degeneracy breaking of the E Raman mode. The breaking of the degeneracy causes the splitting of the $E_{2g}$ mode in the case of the presence of uniaxial strain larger than 0.8%.[21,27] Fig. 3b reports the statistical analysis of the Raman mode separation, obtained by the Raman maps of a single flake shown in ESI Fig. S3.† The Gaussian distribution of the Raman mode separation is obtained by fitting the histogram data. In the case of the flakes synthesized at 810 °C, the distribution is centered at 20.4 $cm^{-1}$ with a FWHM of 0.7 $cm^{-1}$ and it becomes even sharper in the case of the synthesis at 820 °C with a FWHM of 0.5 $cm^{-1}$, being centered at 21.3 $cm^{-1}$. The largest distribution of the Raman mode separation is a FWHM of 1.4 $cm^{-1}$ in the case of the 830 °C grown monolayers, where the Gaussian fitting reveals that the center is at 24.8 $cm^{-1}$. The statistical analysis of the Raman mode separ-

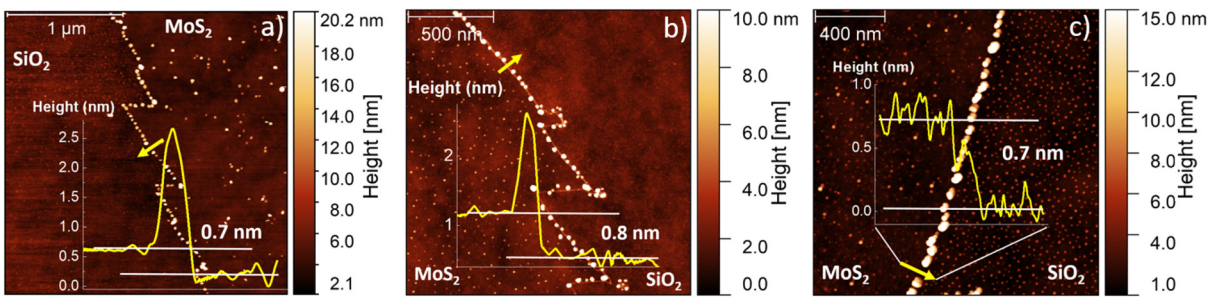


Fig. 2 AFM topographic maps of the edges of the flakes grown at increasing temperatures (a) 810 °C, (b) 820 °C and (c) 830 °C. The height profiles are obtained where the yellow line is reported on each map.

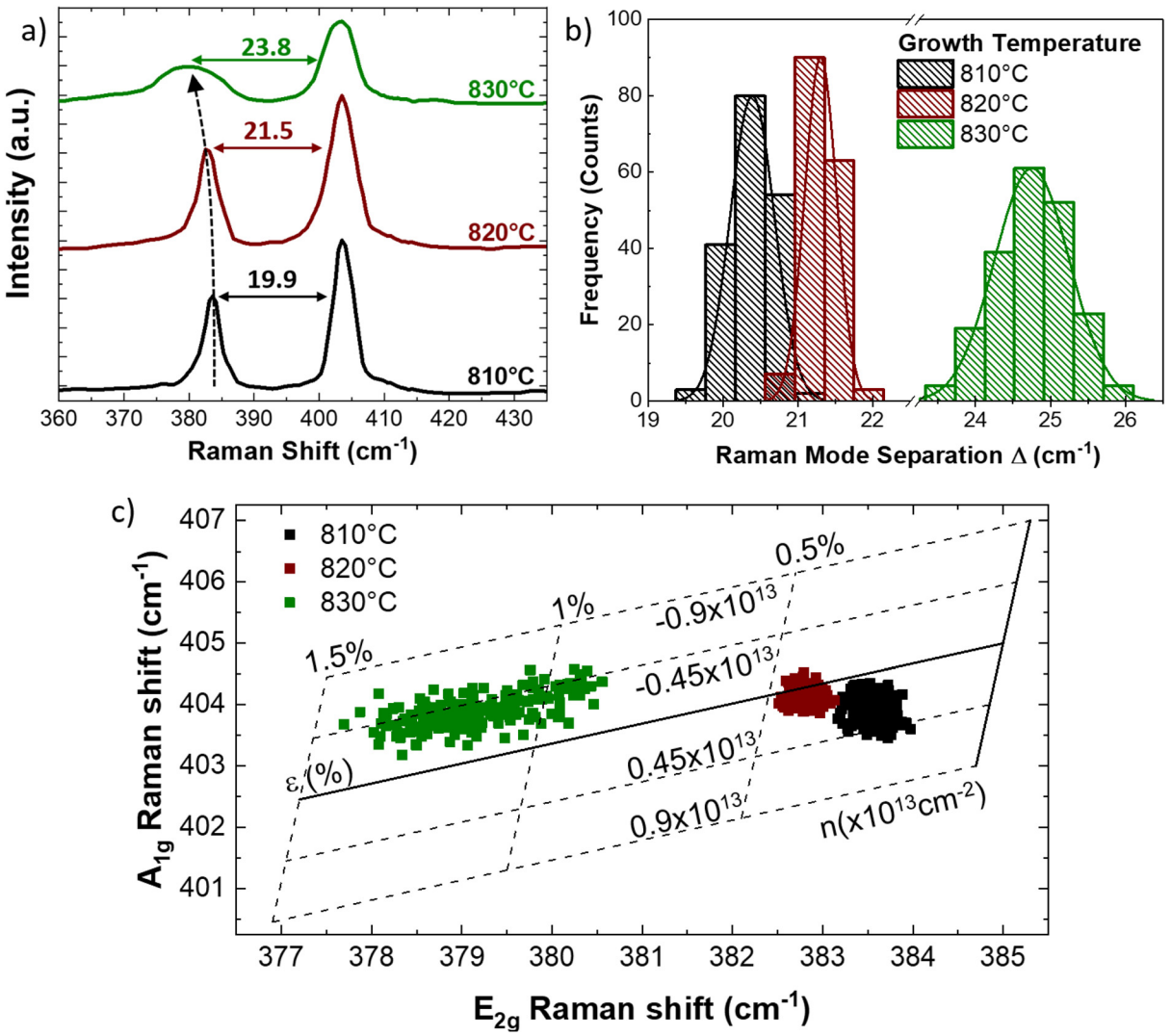


**Fig. 3** (a) Representative Raman spectra of the $MoS_2$ monolayers obtained at increasing temperatures: 810 °C (black line), 820 °C (red line), and 830 °C (green line). The spectra are vertically shifted for the sake of clarity. The Raman mode separation is indicated for each spectrum. (b) Histogram of the Raman mode separation for the different growth temperatures. (c) $MoS_2$ doping/strain correlation plot.

ation is necessary to clarify the discrepancy with the AFM analysis reported in Fig. 2; in fact, all the flakes analyzed are monolayer in nature whereas the Raman results suggest a different number of layers for the increasing growth temperature. This is clear with regard to the different shifts of the two Raman modes when strain is applied to $MoS_2$ because the $E_{2g}$ mode is more affected than the $A_{1g}$ mode, as previously explained. Therefore, we can assess that the presence of built-in strain in the $MoS_2$ synthesis with liquid precursors makes the Raman method unreliable for the evaluation of layer number, using the separation of the vibrational modes. In order to quantify the built-in strain and the modification of doping, we employ the $MoS_2$ correlation plot of the Raman shifts of the $E_{2g}$ and $A_{1g}$ modes, also known as the ε–n system.[60] This method allows to disentangle and to quantify the strain and doping variations and it is normally employed for studying growth induced strain,[61] the effect of different growth substrates[48] or in $MoS_2$ based van der Waals heterostructures.[62,63] The full lines represent the zero strain and zero doping lines, while the dashed lines correspond to iso-strain and the iso-doping lines, calculated following the insights from previous works.[41,64] In addition, it is worth mentioning the importance of the origin of the ε–n system: we set the zero strain and charge neutrality phonon frequencies 385 $cm^{-1}$ for the $E_{2g}$ mode and 405 $cm^{-1}$ for the $A_{1g}$ mode, evaluated in the case of CVD grown $MoS_2$ suspended monolayer membrane.[41] The data regarding the $MoS_2$ monolayers grown at 810 °C present a round distribution revealing an average value of (0.29 ± 0.06)% of tensile strain and an average positive charge concentration of (0.23 ± 0.22) × $10^{13}$ $cm^{-2}$, while in the case of the monolayer synthesized at 820 °C, the data distribution is less dispersed and the average tensile strain increases up to (0.44 ± 0.12)% and the charge concentration decreases close to neutrality, (0.06 ± 0.10) × $10^{13}$ $cm^{-2}$.

 

The average strain reaches its maximum in the case of the $MoS_2$ monolayer obtained at 830 °C, (1.15 ± 0.5)%, albeit the data present a linear distribution along the iso-doping line relative to an electron charge concentration $-0.45 \times 10^{13}$ $cm^{-2}$. In order to clarify the data spreading in the $A_{1g}$ *versus* $E_{2g}$ correlation plot, in the case of the monolayers obtained at 830 °C, the spatial distribution of strain is shown in Fig. 4. The methodology for the development of the strain maps is reported in Fig. S5† with the strain maps of the flakes grown at 810 °C and 820 °C. The Raman spectra in the amorphous carbon range are reported in Fig. S4† showing the absence of any amorphous carbon related peaks that can arise due to organic compounds (*i.e.* iodixanol) in the precursor solution. In addition, the data regarding the $MoS_2$ MLs transferred on a clean $SiO_2$/Si substrate are reported in Fig. S5.†

The strain map of the 830 °C grown monolayer (Fig. 4a) reveals that the strain is partially released in the triangular vertexes of the flake. This finding supports the spreading of the data reported in Fig. 3c. In fact, while in the central part of the flake the strain is above 1%, it decreases to 0.7%–0.8% close to the vertexes of the triangular monolayer. The strain release mechanism is based on the formation of nanocracks in such regions, demonstrated by AFM phase analysis (Fig. 4b). The AFM phase analysis is employed to maximize the contrast of the nanocracks, and the topographical map is reported in Fig S6 of the ESI.† A similar strain release mechanism has been previously reported in the case of $MoS_2$ monolayer exposed to hydrogen or oxygen plasma.[65,66] The similarities rely mainly on the formation of a six-fold hexagonal patterned net of nanocracks. The angle distribution of the lines relative to the edge of the $MoS_2$ crystal has preferential orientations of 0°, 60°, and 120° as shown in Fig. 4b, which indicates that the line patterns are associated with the crystallographic orientation of the $MoS_2$. This effect is important because it demonstrates that the $MoS_2$ monolayer can sustain a limited amount of built-in tensile strain during the growth process, while the strain applied by external procedures can reach 10%.[18] The strain maps of the ML synthesized at 810 °C and 820 °C are reported in Fig. S7.†

Another method for evaluating the strain in atomically thin semiconducting TMDs is the analysis of the photoluminescence (PL) emission. Several previous works have demonstrated the strain dependence of the PL emission energy and intensity.[21,22,27,41,44,67,68] In the case of the $MoS_2$ monolayer, the standard PL spectrum presents two main peaks attributed to the A and B excitons. The emission energy of the A exciton is reported to vary between 1.82 eV and 1.89 eV,[21,27,68,69] while the B exciton energy varies between 1.97 eV and 2.05 eV,[21,27,44,68,69] In our particular case, Fig. 5 presents the representative PL spectra of the $MoS_2$ monolayer grown at increasing temperatures, acquired at the center of the flake. The PL spectrum of 810 °C grown ML shows one sharp peak at 1.86 eV and a faint shoulder in the high energy side, that is at 2.01 eV. On increasing the growth temperature at 820 °C, the A exciton peaks suffer 58% quenching of the integrated PL intensity and a slight red-shift of the emission energy (0.01 eV), peaked at 1.85 eV. The red shift is even higher and the quenching more serious, in the case of the 830 °C grown monolayers; in fact, the PL emission energy shifts down to 1.78 eV and quenching increases to 62%. It is worth noting that the quenching effect is limited by the broadening of the A excitonic PL peak. Fig. 5b resumes the PL A exciton emission energy and the PL integrated intensity as a function of the growth temperature of the $MoS_2$ MLs. We consider a PL energy gauge factor of −99 ± 6 meV per %, measured in the case of biaxial strain of CVD grown MoS2 monolayer,[41] that is in good agreement with the theoretical prediction of 105 meV per %.[70] The biaxial strain, obtained by the PL shift, is 0.4% in the case of the ML grown at 810 °C, while it increases up to 0.5% for the 820 °C synthesized MLs. The biaxial strain is maximized in the case of the ML grown at 830 °C with a value equal to 1.2%. It is worth noting that these values are calculated considering

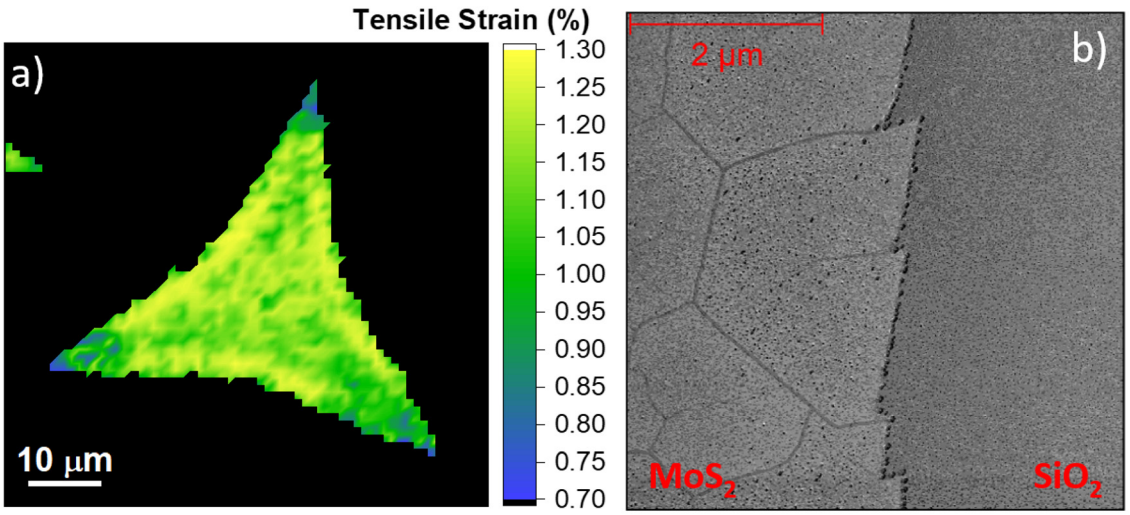


**Fig. 4** Representative strain map of the $MoS_2$ monolayers obtained at 830 °C (panel a) and the AFM phase map of the edge of the flakes (panel b).

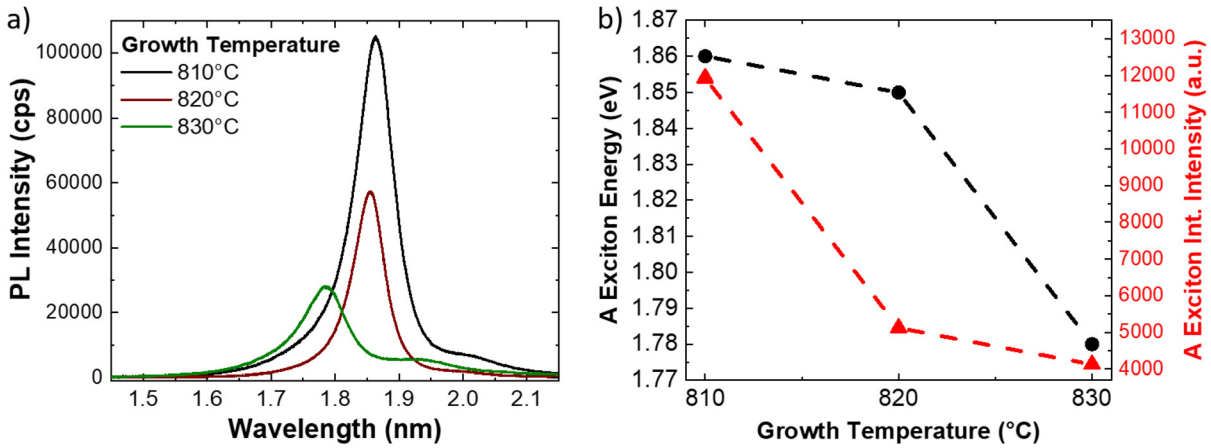


**Fig. 5** (a) Representative PL spectra of the $MoS_2$ monolayers synthesized at 810 °C (black line), 820 °C (red line) and 830 °C (green line), acquired at the center of the flake. (b) Resuming behaviors of the A exciton emission energy (black dots) and PL intensity (red triangles) as a function of the growth temperature. The dashed lines are guides for the reader's eyes.

the peak energy of the A exciton for unstrained $MoS_2$ ML at 1.9 eV.[41,69]

The comparison of the PL spectra obtained at the center and the edge of the 830 °C grown ML is reported in Fig. S8.†

Fig. 6 proposes a mechanism for the large variation of the $MoS_2$ built-in strain with the reduced tuning of the growth temperature. This model is based on three main aspects: (1) the thermal expansion coefficient (TEC) mismatch between the two dimensional material and the substrate during the growth process,[4] (2) the employment of the liquid precursors in the CVD process,[52,61] (3) the strain dependence on the size of the $MoS_2$ ML synthesized at temperatures above 820 °C.[49,71] The direct comparison of the built-in strain values as a function of the temperature with the theoretical TEC induced mismatch for the synthesis of $MoS_2$ on thermal silicon dioxide is shown in Fig. 6a. Thermal silicon dioxide presents a poor linear TEC equal to $\alpha_a = 0.24 \times 10^6\ K^{-1}$ (ref. 72) while $MoS_2$ TEC is equal to $\alpha_a = 7.6 \times 10^6\ K^{-1}$.[73] Based on this TEC mismatch, a degree of built-in tensile strain in the $MoS_2$ ranging from 0.577% at 810 °C to 0.593% at 830 °C can be expected. However, the experimental values show that the applied built-in strain are lower than the theoretical values of the TEC mismatch induced built-in strain in the case of the synthesis at 810 °C and 820 °C. The partial release of strain can be due to the presence of an interfacial layer of $Na_2SiO_3$, as demonstrated by the XPS analysis reported in the ESI (Fig. S9and S10†), related to the use of liquid precursors. This demonstrates that the TEC mismatch has a limited effect on the built-in strain in $MoS_2$ flakes obtained with liquid precursors, while the main effect of the temperature is to increase the size of $MoS_2$ MLs. Therefore, the main cause of large built-in strain in $MoS_2$ ML grown at 830 °C is related to the large lateral size of the sharp-vertex flakes. In fact, tensile strain–size dependence has been previously reported in the case of $MoS_2$ ML grown at a temperature above 820 °C, where the critical size limit for the appearance of strain is 17 μm.[49] In addition, the

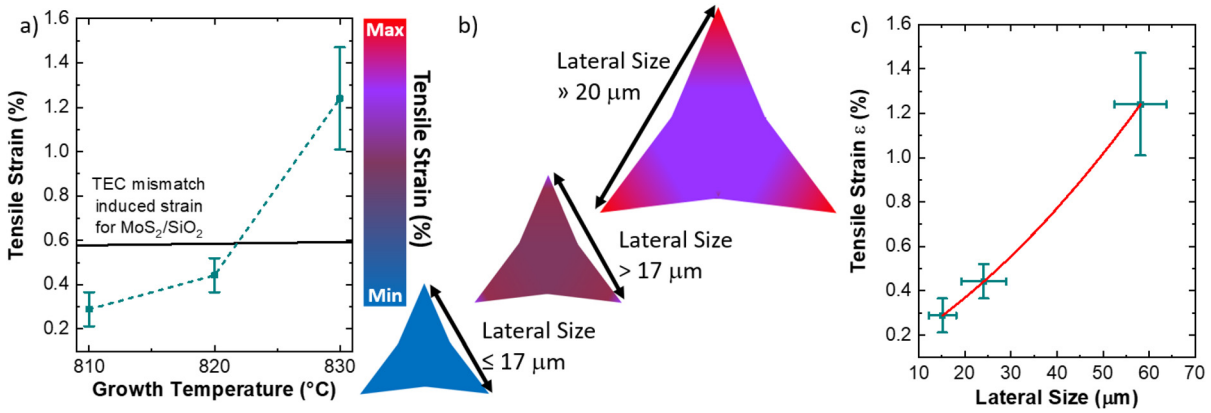


**Fig. 6** (a) Temperature dependent built-in strain values with a direct comparison with the theoretical TCE mismatch strain of the $MoS_2/SiO_2$ interface. (b) Sketch depicting the mechanism of the strain generation in the $MoS_2$ ML with dependence on the flake size. (c) Dependence of the strain on the lateral size of the flake, reporting the polynomial fit.

 

increase in size beyond the critical limit leads to spatial inhomogeneity of the built-in strain, where the edges[74,75] and the vertexes[49,76] are more affected. The possible mechanism is, therefore, resumed in Fig. 6b, where the MLs, obtained at 810 °C present a limited amount of homogeneous strain due to the size close to the critical limit of 17 μm. The $MoS_2$ MLs, presenting a size slightly greater than 17 μm, show an increasing strain in the body of the flake with an enhancement on the flake vertexes (see Fig. S5† for the strain map of 820 °C grown flakes). The built-in strain is maximized with large inhomogeneity in the vertexes when the lateral size of the flake is much larger than 17 μm. The built-in strain value is more than two times the expected values for theoretical $MoS_2/SiO_2$ TEC mismatch induced strain, demonstrating that the size dependent strain is highly enhanced in the case of large-area $MoS_2$ ML. It is worth noting that, in our particular case, the expected built-in strain in the triangular vertexes should be even higher despite the formation of nanocracks partially releasing the accumulated strain. The built-in strain dependence on the ML size and its inhomogeneity can be attributed to the particular DLA growth regime, that gives rise to the fractal saw-toothed edges.[50]

The dependence of the built strain as a function of the ML size is reported in Fig. 6c. The polynomial fitting reveals that the semi-empirical law of the average built-in strain as a function of the average size has parabolic behavior with the following parameters:

$$\varepsilon_{\text{Built-in}} = A \cdot d^2 + B \cdot d \quad (1)$$

where $\varepsilon_{\text{Built-in}}$ is the built-in tensile strain, $d$ is the lateral size of the ML, and $A$ and $B$ are the parameters obtained from the fitting procedures, implying that the intercept is equal to zero and they are $A = 7.3 \times 10^{-5}\%\ \mu m^{-2}$, and $B = 0.017\%\ \mu m^{-1}$. Following this semi-empirical prediction, a $MoS_2$ ML with a lateral size of 100 μm should be affected by a 2.4% strain in the central body of the flake.

## Conclusion

In conclusion, we demonstrate that the built-in strain of $MoS_2$ monolayers, grown on a $SiO_2$/Si substrate by liquid precursor chemical vapor deposition, is mainly dependent on the size of the monolayer. Using correlative analyses of AFM, TEM, Raman and PL, we are able to highlight an inconsistency in the number of layers in $MoS_2$ flakes obtained by liquid precursor CVD. This leads to the identification of built-in strain dependent on the lateral size of $MoS_2$ monolayers. The built-in strain values are close to the prediction of thermal expansion coefficient mismatch for monolayers with a lateral size less than than 20 μm. The built-in strain is drastically increased for 60 μm sized monolayers, leading to 1.2% tensile strain with a partial release of strain close to the monolayer triangular vertexes due to the formation of nanocracks. These results indicate that $MoS_2$ monolayers, grown by liquid precursor CVD, can have a large built-in tensile strain when high growth temperatures (above 820 °C) are used to increase the monolayer size. A semi-empirical model is defined for the possible prediction of the expected built-strain for a certain lateral size of $MoS_2$ monolayers without considering the possible release of strain due to the material cracking. The built-in strain dependence on the ML size and its inhomogeneity are tentatively attributed to the diffusion limited aggregation regime at high temperatures that gives rise to the fractal saw-toothed edges of the $MoS_2$ monolayers.

## Experimental section

The chemicals composing the Mo liquid precursors were AMT (Sigma Aldrich purity 99.98%), NaOH (Carlo Erba) and Optiprep, an iodixanol based component provided by Serumwerk Bernburg AG normally employed in cell cultures.

$MoS_2$ flakes were synthesized under atmospheric pressure in an open tube using S powder with nitrogen as the carrier gas. The employed substrates were commercial 300 nm thick $SiO_2$ coated highly conductive silicon wafer (Siltronic A.G.). Fig. S11† shows a schematic illustration of the CVD reactor, *i.e.* an open tube with a diameter of about 1 inch heated in a two-zone furnace. The sulfur boat is positioned in a low temperature zone ($T$ = 180° C), while the growth substrate, after the spinning process of the Mo precursor solution, is placed in the high temperature zone (810 °C < $T$ < 830 °C).[77,78]

AFM topography and phase maps were collected using a Bruker AFM operated in the scan assist mode. Scanning Raman and photoluminescence spectroscopy were carried out with a Renishaw InVia system, equipped with a confocal microscope, a 532 nm excitation laser and a 2400 line per mm grating (spectral resolution <1 $cm^{-1}$). All the analyses were performed with an 100× objective (NA = 0.85), excitation laser power 500 μW, acquisition time 4 s for each spectrum and a pixel size of 1 μm × 1 μm. The Raman modes were fitted with a Lorentzian peak, except for the $E_{2g}$ mode of the specimen obtained at 830 °C that was fitted with a Voight peak due to the peculiar shape.

The statistical analysis involved analyzing twelve triangular structures, six measured by AFM and six measured by optical microscopy. The Raman scanning spectroscopic analysis was carried out on three different areas across the specimen.

Cross-sectional TEM analysis of a $MoS_2$ flake grown at 830 °C was performed on a TEM-lamella prepared by a Zeiss Auriga Compact Focused Ion Beam (FIB) system. In order to protect the atomically thin layer of $MoS_2$ from damage by the ion beam,[79] the specimen was coated with amorphous carbon in a Balzers CED-010 setup prior to applying the standard procedure of FIB-lamella preparation. The lamella was then observed under a JEOL JEM 2200-FS microscope, operated at 200 kV.

We performed X-ray photoelectron spectroscopy (XPS) in an ultra-high-vacuum (UHV) chamber using a VSW HA100 hemispherical electron energy analyzer with a PSP power supply and control.[80] We used a non-monochromatized Mg Kα X-ray

source (photon at 1253.6 eV), with a final energy resolution at 0.86 eV. The Au 4f 7/2 peak at 84.0 eV has been used as calibration for the binding energy (BE) scale. Core level lineshape analysis has been performed using Voigt functions with a Gaussian to Lorentian ratio of 30%, after the subtraction of a Shirley background. The typical precision for each component's energy position was ±0.05 eV while for the area evaluation it was approximately ±2%.

## Conflicts of interest

There are no conflicts to declare.

## Acknowledgements

The authors wish to thank Prof. R. Fornari (Department of Mathematical, Physical and Computer Sciences, University of Parma) for the useful discussion and support, Dr G. Attolini for his contribution during the CVD growth of $MoS_2$ and Dr G. Bertoni (CNR-Nano, Modena) for his assistance in the carbon coating process prior to the TEM lamella preparation.

## References

1 R. Roldán, A. Castellanos-Gomez, E. Cappelluti and F. Guinea, *J. Phys.: Condens. Matter*, 2015, **27**, 313201.
2 Z. Dai, L. Liu and Z. Zhang, *Adv. Mater.*, 2019, **31**, 1805417.
3 Z. Peng, X. Chen, Y. Fan, D. J. Srolovitz and D. Lei, *Light: Sci. Appl.*, 2020, **9**, 190.
4 G. H. Ahn, M. Amani, H. Rasool, D.-H. Lien, J. P. Mastandrea, J. W. Ager III, M. Dubey, D. C. Chrzan, A. M. Minor and A. Javey, *Nat. Commun.*, 2017, **8**, 608.
5 S. Deng, A. V. Sumant and V. Berry, *Nano Today*, 2018, **22**, 14–35.
6 L. Du, T. Hasan, A. Castellanos-Gomez, G.-B. Liu, Y. Yao, C. N. Lau and Z. Sun, *Nat. Rev. Phys.*, 2021, **3**, 193–206.
7 G. G. Naumis, S. Barraza-Lopez, M. Oliva-Leyva and H. Terrones, *Rep. Prog. Phys.*, 2017, **80**, 96501.
8 J. Du, H. Yu, B. Liu, M. Hong, Q. Liao, Z. Zhang and Y. Zhang, *Small Methods*, 2021, **5**, 2000919.
9 T.-J. Ko, M. Wang, C. Yoo, E. Okogbue, M. A. Islam, H. Li, M. S. Shawkat, S. S. Han, K. H. Oh and Y. Jung, *J. Phys. D: Appl. Phys.*, 2020, **53**, 313002.
10 Y. Qi, M. A. Sadi, D. Hu, M. Zheng, Z. Wu, Y. Jiang and Y. P. Chen, *Adv. Mater.*, 2022, 2205714.
11 S. B. Desai, G. Seol, J. S. Kang, H. Fang, C. Battaglia, R. Kapadia, J. W. Ager, J. Guo and A. Javey, *Nano Lett.*, 2014, **14**, 4592–4597.
12 E. Blundo, M. Felici, T. Yildirim, G. Pettinari, D. Tedeschi, A. Miriametro, B. Liu, W. Ma, Y. Lu and A. Polimeni, *Phys. Rev. Res.*, 2020, **2**, 12024.
13 Y. Wang, C. Cong, W. Yang, J. Shang, N. Peimyoo, Y. Chen, J. Kang, J. Wang, W. Huang and T. Yu, *Nano Res.*, 2015, **8**, 2562–2572.
14 J. Feng, X. Qian, C.-W. Huang and J. Li, *Nat. Photonics*, 2012, **6**, 866–872.
15 S. Z. Uddin, N. Higashitarumizu, H. Kim, I. K. M. R. Rahman and A. Javey, *Nano Lett.*, 2022, **22**, 5316–5321.
16 M. G. Harats, J. N. Kirchhof, M. Qiao, K. Greben and K. I. Bolotin, *Nat. Photonics*, 2020, **14**, 324–329.
17 P. Hernández López, S. Heeg, C. Schattauer, S. Kovalchuk, A. Kumar, D. J. Bock, J. N. Kirchhof, B. Höfer, K. Greben, D. Yagodkin, L. Linhart, F. Libisch and K. I. Bolotin, *Nat. Commun.*, 2022, **13**, 7691.
18 S. Bertolazzi, J. Brivio and A. Kis, *ACS Nano*, 2011, **5**, 9703–9709.
19 Y. Yang, X. Li, M. Wen, E. Hacopian, W. Chen, Y. Gong, J. Zhang, B. Li, W. Zhou, P. M. Ajayan, Q. Chen, T. Zhu and J. Lou, *Adv. Mater.*, 2017, **29**, 1604201.
20 A. Falin, M. Holwill, H. Lv, W. Gan, J. Cheng, R. Zhang, D. Qian, M. R. Barnett, E. J. G. Santos, K. S. Novoselov, T. Tao, X. Wu and L. H. Li, *ACS Nano*, 2021, **15**, 2600–2610.
21 H. J. Conley, B. Wang, J. I. Ziegler, R. F. Haglund, S. T. Pantelides and K. I. Bolotin, *Nano Lett.*, 2013, **13**, 3626–3630.
22 K. He, C. Poole, K. F. Mak and J. Shan, *Nano Lett.*, 2013, **13**, 2931–2936.
23 A. Castellanos-Gomez, R. Roldán, E. Cappelluti, M. Buscema, F. Guinea, H. S. J. van der Zant and G. A. Steele, *Nano Lett.*, 2013, **13**, 5361–5366.
24 L. Mennel, V. Smejkal, L. Linhart, J. Burgdörfer, F. Libisch and T. Mueller, *Nano Lett.*, 2020, **20**, 4242–4248.
25 J. O. Island, A. Kuc, E. H. Diependaal, R. Bratschitsch, H. S. J. van der Zant, T. Heine and A. Castellanos-Gomez, *Nanoscale*, 2016, **8**, 2589–2593.
26 Y. Wang, C. Cong, C. Qiu and T. Yu, *Small*, 2013, **9**, 2857–2861.
27 O. Çakıroğlu, J. O. Island, Y. Xie, R. Frisenda and A. Castellanos-Gomez, *Adv. Mater. Technol.*, 2022, 2201091.
28 M. Zeng, J. Liu, L. Zhou, R. G. Mendes, Y. Dong, M.-Y. Zhang, Z.-H. Cui, Z. Cai, Z. Zhang, D. Zhu, T. Yang, X. Li, J. Wang, L. Zhao, G. Chen, H. Jiang, M. H. Rümmeli, H. Zhou and L. Fu, *Nat. Mater.*, 2020, **19**, 528–533.
29 W. Xu, T. Li, Z. Qin, Q. Huang, H. Gao, K. Kang, J. Park, M. J. Buehler, J. B. Khurgin and D. H. Gracias, *Nano Lett.*, 2019, **19**, 7941–7949.
30 W. Zheng, W. Huang, F. Gao, H. Yang, M. Dai, G. Liu, B. Yang, J. Zhang, Y. Q. Fu, X. Chen, Y. Qiu, D. Jia, Y. Zhou and P. Hu, *Chem. Mater.*, 2018, **30**, 6063–6070.
31 L. Cai, M. J. Shearer, Y. Zhao, Z. Hu, F. Wang, Y. Zhang, K. W. Eliceiri, R. J. Hamers, W. Yan, S. Wei, M. Tang and S. Jin, *J. Am. Chem. Soc.*, 2018, **140**, 10980–10987.
32 C. Choi, M. K. Choi, S. Liu, M. Kim, O. K. Park, C. Im, J. Kim, X. Qin, G. J. Lee, K. W. Cho, M. Kim, E. Joh, J. Lee, D. Son, S.-H. Kwon, N. L. Jeon, Y. M. Song, N. Lu and D.-H. Kim, *Nat. Commun.*, 2017, **8**, 1664.
33 M. Vutukuru, H. Ardekani, Z. Chen, R. L. Wilmington, K. Gundogdu and A. K. Swan, *ACS Appl. Nano Mater.*, 2021, **4**, 8101–8107.

 

34 Q. Wang, J. Maisch, F. Tang, D. Zhao, S. Yang, R. Joos, S. L. Portalupi, P. Michler and J. H. Smet, *Nano Lett.*, 2021, **21**, 7175–7182.
35 C. Palacios-Berraquero, D. M. Kara, A. R.-P. Montblanch, M. Barbone, P. Latawiec, D. Yoon, A. K. Ott, M. Loncar, A. C. Ferrari and M. Atatüre, *Nat. Commun.*, 2017, **8**, 15093.
36 A. Branny, S. Kumar, R. Proux and B. D. Gerardot, *Nat. Commun.*, 2017, **8**, 15053.
37 A. Balgarkashi, V. Piazza, J. Jasiński, R. Frisenda, A. Surrente, M. Baranowski, M. Dimitrievska, D. Dede, W. Kim, L. Güniat, J.-B. Leran, A. Castellanos-Gomez, P. Plochocka and A. Fontcuberta i Morral, *IEEE J. Quantum Electron.*, 2022, **58**, 1–8.
38 J. Jasiński, A. Balgarkashi, V. Piazza, D. Dede, A. Surrente, M. Baranowski, D. K. Maude, M. Banerjee, R. Frisenda, A. Castellanos-Gomez, A. Fontcuberta i Morral and P. Plochocka, *2D Mater.*, 2022, **9**, 45006.
39 S. Kumar, A. Kaczmarczyk and B. D. Gerardot, *Nano Lett.*, 2015, **15**, 7567–7573.
40 S. Manzeli, A. Allain, A. Ghadimi and A. Kis, *Nano Lett.*, 2015, **15**, 5330–5335.
41 D. Lloyd, X. Liu, J. W. Christopher, L. Cantley, A. Wadehra, B. L. Kim, B. B. Goldberg, A. K. Swan and J. S. Bunch, *Nano Lett.*, 2016, **16**, 5836–5841.
42 F. Colangelo, A. Morandi, S. Forti, F. Fabbri, C. Coletti, F. V. Di Girolamo, A. Di Lieto, M. Tonelli, A. Tredicucci, A. Pitanti and S. Roddaro, *Appl. Phys. Lett.*, 2019, **115**, 183101.
43 H. Kim, G. H. Ahn, J. Cho, M. Amani, J. P. Mastandrea, C. K. Groschner, D.-H. Lien, Y. Zhao, J. W. Ager, M. C. Scott, D. C. Chrzan and A. Javey, *Sci. Adv.*, 2022, **5**, eaau4728.
44 Z. Liu, M. Amani, S. Najmaei, Q. Xu, X. Zou, W. Zhou, T. Yu, C. Qiu, A. G. Birdwell, F. J. Crowne, R. Vajtai, B. I. Yakobson, Z. Xia, M. Dubey, P. M. Ajayan and J. Lou, *Nat. Commun.*, 2014, **5**, 5246.
45 K. Wang, A. A. Puretzky, Z. Hu, B. R. Srijanto, X. Li, N. Gupta, H. Yu, M. Tian, M. Mahjouri-Samani, X. Gao, A. Oyedele, C. M. Rouleau, G. Eres, B. I. Yakobson, M. Yoon, K. Xiao and D. B. Geohegan, *Sci. Adv.*, 2023, **5**, eaav4028.
46 J. Wang, M. Han, Q. Wang, Y. Ji, X. Zhang, R. Shi, Z. Wu, L. Zhang, A. Amini, L. Guo, N. Wang, J. Lin and C. Cheng, *ACS Nano*, 2021, **15**, 6633–6644.
47 T. H. Ly, S. J. Yun, Q. H. Thi and J. Zhao, *ACS Nano*, 2017, **11**, 7534–7541.
48 W. H. Chae, J. D. Cain, E. D. Hanson, A. A. Murthy and V. P. Dravid, *Appl. Phys. Lett.*, 2017, **111**, 143106.
49 L. Lei, Y. Lun, F. Cao, L. Meng, S. Xing, J. Guo, H. Dong, S. Gu, K. Xu, S. Hussain, Y. J. Li, Y. Sugawara, F. Pang, W. Ji, J. Hong, R. Xu and Z. Cheng, *Nanotechnology*, 2021, **32**, 465703.
50 J. Li, M. Chen, C. Zhang, H. Dong, W. Lin, P. Zhuang, Y. Wen, B. Tian, W. Cai and X. Zhang, *Adv. Mater.*, 2019, **31**, 1902431.
51 Y. Wan, H. Zhang, K. Zhang, Y. Wang, B. Sheng, X. Wang and L. Dai, *ACS Appl. Mater. Interfaces*, 2016, **8**, 18570–18576.
52 H. Kim, G. H. Han, S. J. Yun, J. Zhao, D. H. Keum, H. Y. Jeong, T. H. Ly, Y. Jin, J.-H. Park, B. H. Moon, S.-W. Kim and Y. H. Lee, *Nanotechnology*, 2017, **28**, 36LT01.
53 Y.-H. Lee, X.-Q. Zhang, W. Zhang, M.-T. Chang, C.-T. Lin, K.-D. Chang, Y.-C. Yu, J. T.-W. Wang, C.-S. Chang, L.-J. Li and T.-W. Lin, *Adv. Mater.*, 2012, **24**, 2320–2325.
54 Y. Okuno, O. Lancry, A. Tempez, C. Cairone, M. Bosi, F. Fabbri and M. Chaigneau, *Nanoscale*, 2018, **10**, 14055–14059.
55 E. Rotunno, M. Bosi, L. Seravalli, G. Salviati and F. Fabbri, *Nanoscale Adv.*, 2020, **2**, 2352–2362.
56 F. Giannazzo, M. Bosi, F. Fabbri, E. Schilirò, G. Greco and F. Roccaforte, *Phys. Status Solidi RRL*, 2020, **14**, 1900393.
57 H. Li, Q. Zhang, C. C. R. Yap, B. K. Tay, T. H. T. Edwin, A. Olivier and D. Baillargeat, *Adv. Funct. Mater.*, 2012, **22**, 1385–1390.
58 C. Lee, H. Yan, L. E. Brus, T. F. Heinz, J. Hone and S. Ryu, *ACS Nano*, 2010, **4**, 2695–2700.
59 C. Rice, R. J. Young, R. Zan, U. Bangert, D. Wolverson, T. Georgiou, R. Jalil and K. S. Novoselov, *Phys. Rev. B: Condens. Matter Mater. Phys.*, 2013, **87**, 81307.
60 A. Michail, N. Delikoukos, J. Parthenios, C. Galiotis and K. Papagelis, *Appl. Phys. Lett.*, 2016, **108**, 173102.
61 A. Michail, J. Parthenios, D. Anestopoulos, C. Galiotis, M. Christian, L. Ortolani, V. Morandi and K. Papagelis, *2D Mater.*, 2018, **5**, 35035.
62 G. Ciampalini, F. Fabbri, G. Menichetti, L. Buoni, S. Pace, V. Mišeikis, A. Pitanti, D. Pisignano, C. Coletti, A. Tredicucci and S. Roddaro, *ACS Nano*, 2022, **16**, 1291–1300.
63 R. Rao, A. E. Islam, S. Singh, R. Berry, R. K. Kawakami, B. Maruyama and J. Katoch, *Phys. Rev. B*, 2019, **99**, 195401.
64 B. Chakraborty, A. Bera, D. V. S. Muthu, S. Bhowmick, U. V. Waghmare and A. K. Sood, *Phys. Rev. B: Condens. Matter Mater. Phys.*, 2012, **85**, 161403.
65 J.-Y. Lee, J. H. Kim, Y. Jung, J. C. Shin, Y. Lee, K. Kim, N. Kim, A. M. van der Zande, J. Son and G.-H. Lee, *Commun. Mater.*, 2021, **2**, 80.
66 G. Ye, Y. Gong, J. Lin, B. Li, Y. He, S. T. Pantelides, W. Zhou, R. Vajtai and P. M. Ajayan, *Nano Lett.*, 2016, **16**, 1097–1103.
67 F. Carrascoso, H. Li, R. Frisenda and A. Castellanos-Gomez, *Nano Res.*, 2021, **14**, 1698–1703.
68 C. R. Zhu, G. Wang, B. L. Liu, X. Marie, X. F. Qiao, X. Zhang, X. X. Wu, H. Fan, P. H. Tan, T. Amand and B. Urbaszek, *Phys. Rev. B: Condens. Matter Mater. Phys.*, 2013, **88**, 121301.
69 K. F. Mak, C. Lee, J. Hone, J. Shan and T. F. Heinz, *Phys. Rev. Lett.*, 2010, **105**, 136805.
70 G. Plechinger, A. Castellanos-Gomez, M. Buscema, H. S. J. van der Zant, G. A. Steele, A. Kuc, T. Heine, C. Schüller and T. Korn, *2D Mater.*, 2015, **2**, 15006.
71 S. Cortijo-Campos, C. Prieto and A. De Andrés, *Nanomaterials*, 2022, 12.
72 C. Tsou, Y.-S. Huang, H.-C. Li and T.-H. Lai, *Sens. Mater.*, 2005, **17**, 441–451.

73 L. Zhang, Z. Lu, Y. Song, L. Zhao, B. Bhatia, K. R. Bagnall and E. N. Wang, *Nano Lett.*, 2019, **19**, 4745–4751.
74 Y. Chen, W. Deng, X. Chen, Y. Wu, J. Shi, J. Zheng, F. Chu, B. Liu, B. An, C. You, L. Jiao, X. Liu and Y. Zhang, *Nano Res.*, 2021, **14**, 2314–2320.
75 S. Luo, C. P. Cullen, G. Guo, J. Zhong and G. S. Duesberg, *Appl. Surf. Sci.*, 2020, **508**, 145126.
76 S. Kataria, S. Wagner, T. Cusati, A. Fortunelli, G. Iannaccone, H. Pandey, G. Fiori and M. C. Lemme, *Adv. Mater. Interfaces*, 2017, **4**, 1700031.
77 I. Irfan, S. Golovynskyi, M. Bosi, L. Seravalli, O. A. Yeshchenko, B. Xue, D. Dong, Y. Lin, R. Qiu, B. Li and J. Qu, *J. Phys. Chem. C*, 2021, **125**, 4119–4132.
78 L. Seravalli, M. Bosi, P. Fiorenza, S. E. Panasci, D. Orsi, E. Rotunno, L. Cristofolini, F. Rossi, F. Giannazzo and F. Fabbri, *Nanoscale Adv.*, 2021, **3**, 4826–4833.
79 A. B. Andersen, A. Shivayogimath, T. Booth, S. Kadkhodazadeh and T. W. Hansen, *Phys. Status Solidi*, 2020, **257**, 2000318.
80 R. Tatti, L. Aversa, R. Verucchi, E. Cavaliere, G. Garberoglio, N. M. Pugno, G. Speranza and S. Taioli, *RSC Adv.*, 2016, **6**, 37982–37993.